The Astrophysical Journal, 642:541–553, 2006 May 1

FLUX ROPE MODEL OF THE 2003 OCTOBER 28–30 CORONAL MASS EJECTION AND INTERPLANETARY CORONAL MASS EJECTION

J. Krall
Naval Research Laboratory, Plasma Physics Division, Code 6790, Washington, DC 20375-5000

V. B. Yurchyshyn
Big Bear Solar Observatory, 40386 North Shore Lane, Big Bear City, CA 92314

S. Slinker
Naval Research Laboratory, Plasma Physics Division, Code 6790, Washington, DC 20375-5000

R. M. Skoug
Los Alamos National Laboratory, Space Science and Applications, Group ISR-1, MS D466, Los Alamos, NM 87545

AND

J. Chen
Naval Research Laboratory, Plasma Physics Division, Code 6790, Washington, DC 20375-5000
Received 2005 September 30; accepted 2005 December 30

ABSTRACT

A numerical model of an erupting solar flux rope is shown to reproduce both quantitative near-Sun properties of the 2003 October 28 coronal mass ejection and the timing, strength, and orientation of the fields measured in situ at 1 AU. Using a simple erupting flux rope model, we determine the best-fit parameters for this event. Our analysis shows that the orientation of the magnetic axis of the flux rope in this case rotates smoothly through approximately 50° as the flux rope apex expands from the solar surface to 1 AU. Using a global magnetospheric simulation code, we further show that the resulting model solar wind properties at 1 AU produce a magnetospheric response comparable to that computed using the actual solar wind data.

Subject headings: solar-terrestrial relations — Sun: coronal mass ejections (CMEs) — Sun: magnetic fields

Online material: color figure

1. INTRODUCTION

Any practical model of the dynamics of a coronal mass ejection (CME) and its interplanetary counterpart, an "interplanetary coronal mass ejection" (ICME; Lindsay et al. 1999), must conform to available observational constraints. These constraints typically include the source location, the dynamics of the CME material, and, for Earth-directed events, in situ measurements of the solar wind. Further observations are often available and may provide additional useful constraints for the models now, in specific cases, and in the future, as the models improve. Eventually, it is hoped that near-Sun CME measurements will provide inputs for a practical CME model, with the output being a rapid prediction of the subsequent solar wind parameters at 1 AU. Such a model could provide improved forecasts of "space weather" near Earth.

The 2003 October 28–30 CME/ICME event is particularly illustrative of the effects of space weather on Earth's environment, as it affected near-Earth spacecraft operations and was associated with electron density enhancements in the plasmasphere (Chi et al. 2005), in the $L = 2$ radiation belt (Looper et al. 2005), and in the ionosphere (Tsurutani et al. 2005). It was also associated with a ground-level enhancement of energetic neutrons (Bieber et al. 2005), daytime auroral activity over the continental US (Pallamraju & Chakrabarti 2005), and significant mesospheric ozone depletion (Seppälä et al. 2004; Degenstein et al. 2005).

In this paper, we show that the erupting flux rope (EFR) model (Chen & Garren 1993; Chen 1996; Krall et al. 2000) can, with small modifications, reproduce many details of the CME/ICME event of 2003 October 28–30. We further show that the resulting model solar wind properties at 1 AU produce a magnetospheric response that is comparable to that produced by the actual solar wind. Here the magnetospheric response to model solar wind (or observed solar wind) inputs is computed using the time-dependent, global, three-dimensional, magnetohydrodynamic (MHD), Lyon-Fedder-Mobarry (LFM) magnetospheric simulation model (Lyon et al. 2004).

Of particular interest to us is the fact that a model-data comparison with a halo CME event places geometrical constraints on the EFR model that were not present in previous model-data comparisons for limb events. We are further interested in the relationship between the CME near the Sun and the ICME at 1 AU in terms of orientation, near-Sun and near-Earth velocities, and timing. For this rather fast event (peak observed velocity >2000 km s^{-1}), the simple model does an excellent job of reproducing the timing, strength, and orientation of the observed magnetic fields at 1 AU.

To place this work in context, we note that numerous studies of ICME dynamics have been performed in one dimension (Gosling & Riley 1996), two dimensions (Cargill et al. 1995; Wu et al. 1999; Riley et al. 2003), and three dimensions (Manchester et al. 2004). In the two-dimensional and three-dimensional cases the ICME is assumed to have a flux rope magnetic geometry. We note that the two-dimensional and three-dimensional studies include dynamics that lead to distortions of the transverse cross section of the flux rope; these forces are not present in the EFR model that is used here. In one case (Riley et al. 2003), two-dimensional model results were compared to multispacecraft in situ data at 1 and 5 AU in order to estimate the significance of these distortions. While these multidimensional simulation models have provided

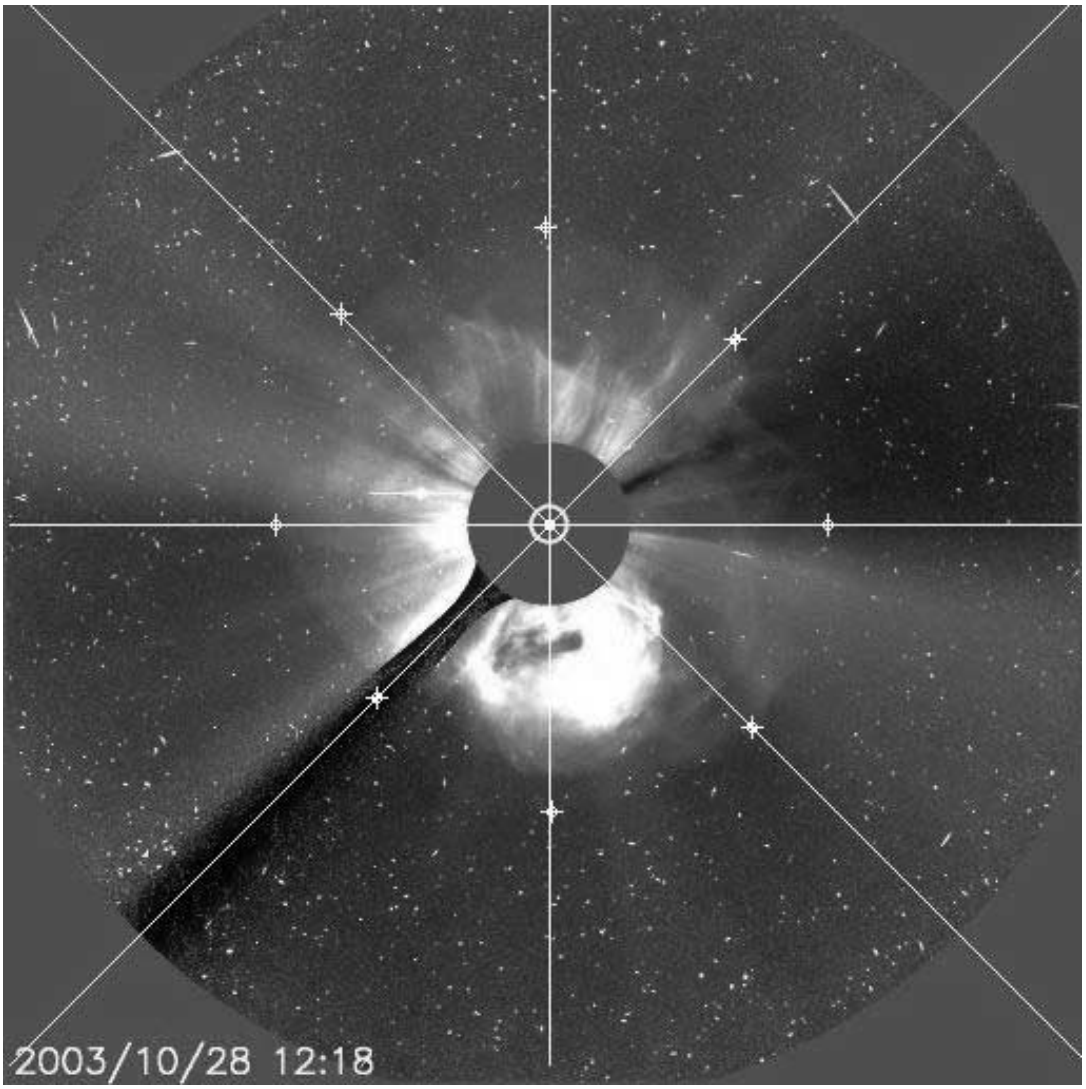

FIG. 1.—Halo CME image from 2003 October 28 at 12:18 UT. Halo measurement positions, at intervals of 45°, are indicated. [*See the electronic edition of the Journal for a color version of this figure.*]

useful (but largely untested) insight into ICME dynamics in the heliosphere, none of these modeling efforts have been applied in such as way as to match both the observed CME halo dynamics and ICME measurements for any specific event. At present, the EFR model is complementary to these two-dimensional and three-dimensional studies in that the EFR model does not show how the flux rope configuration comes about; the flux rope is assumed. The EFR model also does not address many details of the eruption process, such as the processes associated with the introduction of large amounts of "twisted" magnetic flux into the flux rope before or during eruption; the helicity increase is simply specified. The EFR model has an advantage over two-dimensional CME studies in that the magnetic driving force, the $\boldsymbol{J} \times \boldsymbol{B}$ force, has the correct three-dimensional scaling properties (Chen & Krall 2003). The greatest advantage of this model, of course, is that it can be run quickly enough that both near-Sun and near-Earth model-data "matches" can be obtained via a trial-and-error process. The results for any given event are quantitative estimates of CME or ICME densities, velocities, fields, magnetic fluxes, etc., at any point from the solar surface to 1 AU and beyond.

By making use of the relatively simple EFR model, we are able to model a Sun–solar system connection (S3C) event from Sun to Earth. In so doing we find that the halo CME geometry is indeed reproduced by an erupting flux rope and provide further confirmation of a strong correlation between the orientation of the preeruption magnetic fields in an active region and those in the corresponding ICME at Earth (Rust 1994; Yurchyshyn et al. 2001, 2005; Hu et al. 2005) for an ICME that exhibits smoothly varying magnetic-cloud–like field structure (Burlaga et al. 1981; Burlaga 1988). We also find that the model fields at 1 AU in this case can drive a magnetospheric response similar to that expected from the actual, noisy solar wind. This latter point is of interest because it suggests that this relatively simple model might later be applied so as to produce useful predictions of space weather.

The remainder of this paper proceeds as follows. Observations of the event are presented in § 2, the flux rope geometry, model details, and model-data comparisons for the near-Sun and near-Earth regions are presented in § 3, and § 4 concludes this paper with a discussion of key results.

2. THE 2003 OCTOBER 28–30 CME/ICME EVENT

The 2003 October 28 CME, which first appeared in the field of view of the *Solar and Heliospheric Observatory* (*SOHO*) Large Angle and Spectrometric Coronagraph Experiment (LASCO) C2 coronagraph (Brueckner et al. 1995) at 11:30 UT, was an extremely fast halo CME event associated with a simultaneous

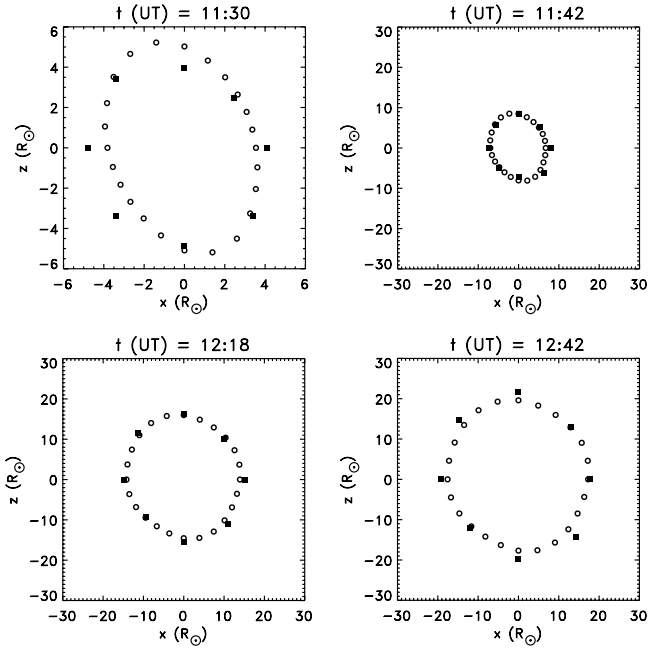

FIG. 2.—Halo measurements and model results for 2003 October 28 at 11:30, 11:42, 12:18, and 12:42 UT. The trace of the projected halo from the model CME is indicated by the open circles; filled squares correspond to measured points from coronagraph images, such as those indicated in Fig. 1.

X-class flare and, 25 hr later, the appearance of an ICME at 1 AU. Because this event has been described elsewhere (Seppälä et al. 2004; Skoug et al. 2004; Woods et al. 2004; Zurbuchen et al. 2004; Bieber et al. 2005; Chi et al. 2005; Degenstein et al. 2005; Hu et al. 2005; Gopalswamy et al. 2005; Looper et al. 2005; Pallamraju & Chakrabarti 2005; Tsurutani et al. 2005; Yurchyshyn et al. 2005), we limit our discussion of the observations to solar surface observations that provide model inputs and near-Sun (coronagraph) and near Earth (in situ) observational results that must be reproduced in order for the model to be deemed successful.

In this very fast event, the erupting structure expanded so rapidly that it was captured in only one LASCO C2 white-light coronagraph image (11:30 UT) and four LASCO C3 white-light coronagraph images (11:42, 12:18, 12:42, and 13:43 UT). The LASCO C3 image data from 13:43 UT were obscured by the effect of energetic particles hitting the LASCO detector and was not used in this study.

A LASCO C3 image from 12:18 UT is shown in Figure 1. This white-light image shows the total brightness of Thomson-scattered light from free electrons. The CME can be seen as an irregularly shaped "halo" around the occulting disk; a circle at the center of the image indicates the size and location of the Sun. Below and slightly to the west, a bright, looplike feature appears. Directly opposite, indications of a similar, but fainter, structure can also be seen. These and several other features within the halo persisted from frame to frame as the CME expanded, qualitatively maintaining their geometrical relationships to each other and to the surrounding faint halo.

To quantify the observed CME morphology—the size, shape, and orientation of the halo—eight points, evenly spaced in position angle, were measured along the outer edge of the halo in each image. In Figure 1, these position angles are indicated by straight lines, and the measured points are indicated by crosses. At each angle, the edge of the halo is chosen to be the outermost point on the overall expanding CME structure. Figure 2 shows

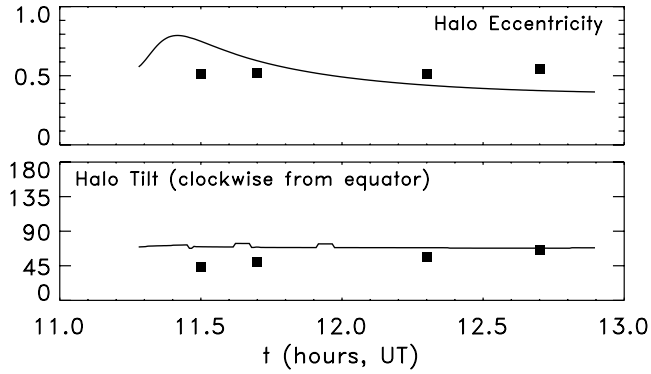

FIG. 3.—Measured halo evolution (*points*) and corresponding model results (*curves*). *Top:* Halo ellipse eccentricity. *Bottom:* Tilt, in the clockwise direction, of the halo ellipse major axis relative to the solar equator.

these measured points from the C2 image and the three C3 images as filled squares (the open circles are model results to be discussed below). We see that the shape of the measured halo evolves slowly as it expands and that the orientation of the major axis of the observed halo ellipse becomes somewhat more vertical with time. These properties can be quantified by fitting an ellipse to the halo points and plotting the halo ellipse eccentricity and tilt angle. This is shown in Figure 3, where the eccentricity and tilt angle are plotted as points in the top and bottom panels, respectively. Here the tilt increases in the clockwise direction relative to the solar equator. Figure 3 also includes curves, which are model results that are further discussed below.

We now consider the observations of the source region for this event. Figure 4 shows a magnetogram image from the Michelson Doppler Imager (MDI) instrument (Scherrer et al. 1995) at 10:00 UT of the large active region that was the source of the eruption. The magnetogram shows a southward-polarity region (*black*; field directed away from the viewer) northwest of a large northward-polarity region (*white*). Another southward-polarity region is located southeast of the white area. A narrow black horizontal feature appears to connect the two southward-polarity regions, bisecting the white area in the image. If the horizontal feature is ignored, one might imagine that there are two major neutral lines in the image, one northwest of the white region, extending from northeast to southwest, and one southeast of the white region, oriented roughly parallel to the northwest neutral line.

Figure 5 shows several EUV Imaging Telescope (EIT; Delaboudinière et al. 1995) images, taken at wavelength 195 Å on 2003 October 28 at 10:24, 10:48, 11:12, and 12:24 UT. These images, selected from a total of 11 such images taken during this time, show considerable activity. At 10:24 UT, we see two bright

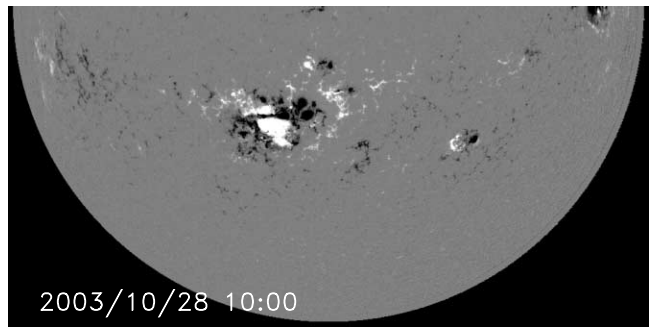

FIG. 4.—Magnetogram from the MDI instrument on 2003 October 28 at 10:00 UT.

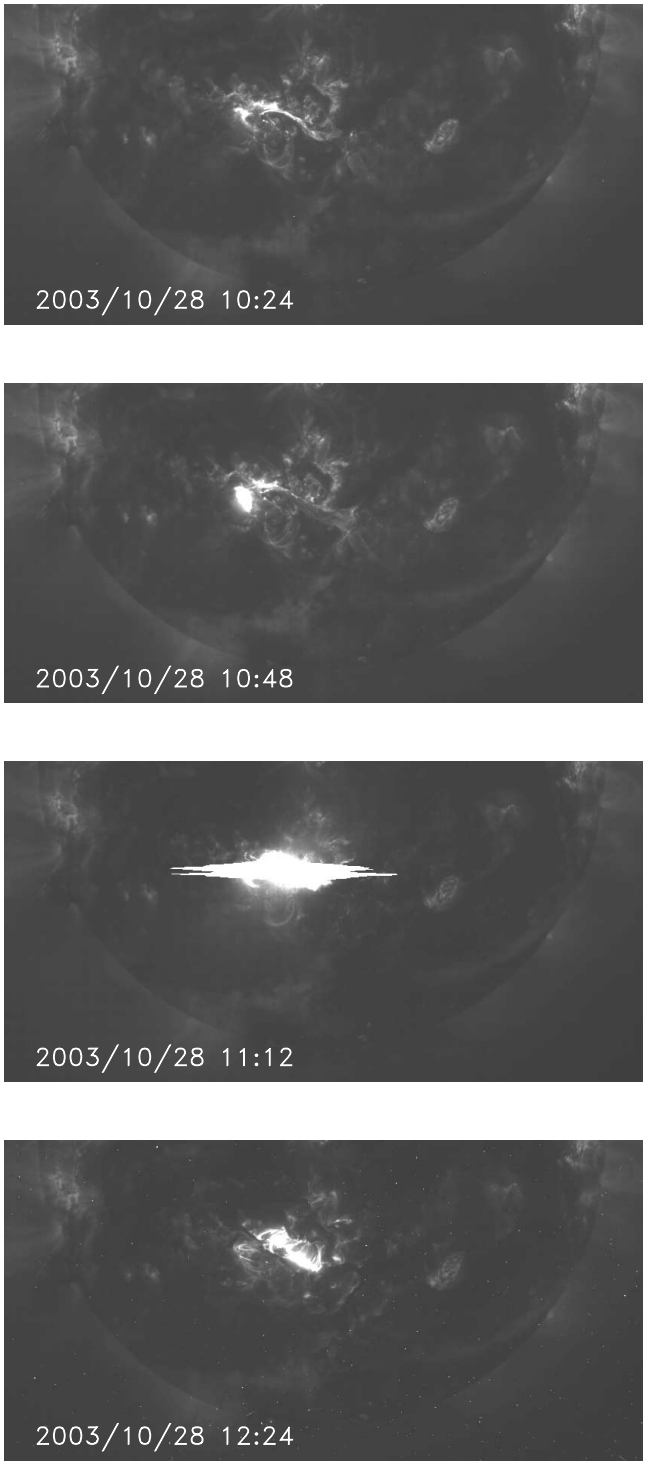

FIG. 5.—Selected EIT images from 2003 October 28.

features, each apparently associated with one of the two major neutral lines identified in the magnetogram (Fig. 4), along with fainter features that seem to connect the two neutral lines. At 10:48, there is flaring over the southeast neutral line. At 11:12 UT the X17 flare is evident over most of the active region; light from this flare was intense enough to saturate the EIT detector, leading to image artifacts in the form of bright white horizontal features. At 12:24 UT, a bright, posteruption arcade can be seen, oriented along the northwest neutral line. Based on the timing of the flare in the 11:12 UT EIT image, on the location of the corresponding active region neutral line (northwest of the white

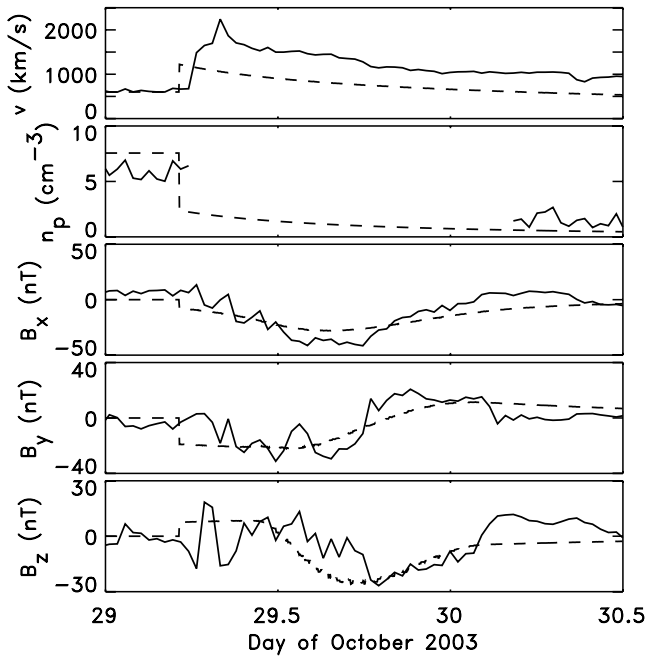

FIG. 6.—Solar wind data from the MAG and SWEPAM instruments on the *ACE* spacecraft for 2003 October 29–30 (*solid curves*). Also shown are corresponding model results (*dashed curves*). Note that there is a data dropout in the *ACE* SWEPAM density from October 29 06:20 UT to October 30 04:22 UT. Field components are in GSE coordinates.

northward-polarity region in the magnetogram; Fig. 4), and on the location of the postevent loops in the 12:24 UT EIT image (Fig. 5), we place the source of the eruption at 22° below the equator and 10° toward the east limb, relative to Sun center.

Figure 6 shows solar wind data at 1 AU (*solid curves*) as measured by the Solar Wind Electron, Proton, and Alpha Monitor (SWEPAM; McComas et al. 1998) and Magnetic Field Experiment (MAG; Smith et al. 1998) instruments on the *Advanced Composition Explorer* (*ACE*) spacecraft for this event. During normal operations, SWEPAM collects data every 64 s at energies around the solar wind peak energy. During energetic particle events, as during parts of this event, the tracking of the solar wind peak energy can fail, and valid data are not collected in this mode. However, data are also collected once every half-hour over a broad energy range, and these were the only measurements available for portions of this event. Because of the reduced measurement resolution, these values have large uncertainties relative to the normal mode SWEPAM data. (For more details, see Skoug et al. 2004.) Note that there was a data dropout in the SWEPAM proton density from October 29 06:20 UT to October 30 04:22 UT. Skoug et al. (2004) report proton density values between 1 and 3 cm^{-3} during the period of the data dropout but with high uncertainty.

Because the ICME temperature is rather high relative to typical solar wind temperatures (see Fig. 3 of Skoug et al. 2004), it may not be appropriate to refer to this ICME as a magnetic cloud (Burlaga et al. 1981; Burlaga 1988). Nevertheless, the ICME is cloudlike in all other respects, with a smoothly rotating flux rope field structure and a relatively low density. An analytical reconstruction of the global field structure of this ICME by Hu et al. (2005) further verifies its flux rope structure. This ICME features a velocity of over 2000 km s^{-1} and an interplanetary (IP) shock at its leading edge. The peak southward magnetic field at *ACE* was −68 nT in the IP shock and −30 nT in the flux rope (Skoug et al. 2004).

3. MODEL RESULTS

In modeling this CME/ICME event, we endeavor to reproduce both the near-Sun CME morphology and dynamics, as observed in coronagraph images, and the timing and characteristics of the near-Earth ICME. We are particularly interested in further testing the hypothesized relationship between the expanding magnetic geometry of the CME and the resulting ICME characteristics at 1 AU.

Here we apply the erupting flux rope (EFR) model (Chen & Garren 1993; Chen 1996; Krall et al. 2000), but with modifications to the flux rope geometry and to the numerical description of the momentum transfer (drag) between the flux rope and the solar wind. The former was required to obtain accurate halo CME morphology, while the latter was introduced to better reflect our current understanding of the connection between the observed electron density, which is captured in coronagraph images, and the underlying flux rope field.

The correspondences between the observed electron density structure and the underlying model magnetic field, which have been shown to work well for "flux rope CME" limb events (Chen et al. 1997, 2000; Wood et al. 1999; Krall et al. 2001), are further tested in this study. As before, we conjecture that the "cavity," which is observed in limb CMEs, corresponds to a density depletion on and around the curved axis of the flux rope (Chen et al. 2000; Krall & Chen 2005) and that this density depletion corresponds to a "current channel" (Chen & Garren 1993; Chen 1996) where the bulk of the current flows within the flux rope. It is this central current channel that provides the model magnetic-cloud–like fields at 1 AU.

3.1. *An Updated Model Geometry for Flux Rope CME Events*

In this paper, we use an updated version of the EFR model described in Chen (1996) and Krall et al. (2000). Here the model has been extended to better model Earth-directed "halo CME" events. As before, the model follows the motion of the apex of a three-dimensional flux rope that has footpoints rooted below the photosphere. As before, the model computes the evolution of the apex height above the photosphere $Z(t)$ and the current-channel radius $a(t)$ at the apex of the flux rope. As before, the bulk of the current flows within this current channel and supports fields that are assumed to be significant, relative to ambient solar wind fields, out to a local radius of $2a$. In the updated model, however, the flux rope geometry has an elliptical shape, as in Figure 7, instead of the previously used circular shape (Fig. 1 of Chen 1996). We refer to the ellipse traced out by the axis of the model flux rope, shown in Figure 7*b*, as the flux rope ellipse.

The primary model outputs at each model time step are Z ($\simeq 2R_1$ in Fig. 7) and a, which is related to the observed density width d by $a = d/4$ (see Fig. 7*a*). This model-data correspondence between a and d has been used consistently throughout all of our CME event studies. These previous model-data comparisons generally focused on limb events that showed "evidence of a magnetic geometry corresponding to a flux rope" (Chen et al. 1997). These events typically featured a prominent round "rim" expanding and moving outward from the Sun, while additional features, "legs," persistently connected the rim feature to the solar disk. Because these previous studies focused on events in which the flux rope geometry was viewed axially, as illustrated in Figure 7*a*, the resulting morphologies would not have been affected if the flux rope geometry had been assumed to be elliptical rather than circular. Thus, the previous results remain valid, at least qualitatively, even if further studies continue to support the idea that flux rope–CME geometry is approximately elliptical.

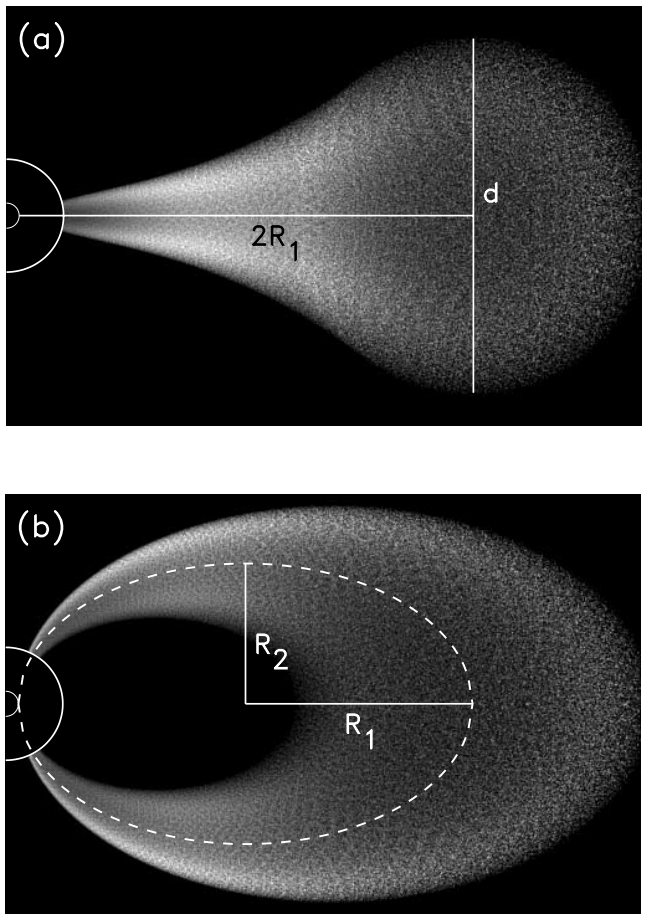

FIG. 7.—Synthetic coronagraph images of the model flux rope CME at 12:18 UT showing (*a*) axial and (*b*) broadside views. Views correspond to what might be seen with a large enough coronagraph field of view (the *x*-axis extends from 0 to 50 $R_\odot$). The flux rope axis is an ellipse with eccentricity $\epsilon = 0.78$ and major diameter $2R_1 = 35.8\ R_\odot$. At this time, the width at the apex is $d = 28.2\ R_\odot$.

The equations for the circular case are given by Chen (1996, eqs. [2] and [9] and references therein) and repeated, with notation closer to what is used in the present paper, by Krall et al. (2000, eqs. [2] and [8]). Note that similar analyses, also for the circular case, have been performed by Lin et al. (1998, eq. [16]) and Titov & Démoulin (1999, eq. [5]). The modified equations used in the present study are given in the Appendix.

When modeling a halo CME, the underlying geometry is of particular interest because observed motion in the plane of the sky can differ significantly from the motion of the Earth-directed CME mass. In the updated EFR model, the flux rope is a simple construct that allows us to specify its geometry in terms of three simple parameters, flux rope ellipse eccentricity $\epsilon = [1-(R_2/R_1)^2]^{1/2}$, axial aspect ratio $\Lambda_a = 2R_1/d$, and the overall size. The latter two parameters are related to model outputs $a(t)$ and $Z(t)$, while ϵ is a model input and is adjusted to obtain an optimum model-data match. Of course, it is the underlying three-dimensional geometry that dictates the properties of the corresponding two-dimensional images, such as the shape of the observed halo ellipse. For example, the model flux rope of Figure 7 has $\epsilon = 0.78$ and $\Lambda_a \simeq 1.3$. When viewed axially, as in Figure 7*a*, the CME has a vertical width $d = 28.2\ R_\odot$, and when viewed broadside (Fig. 7*b*), it has a vertical width of $31.4\ R_\odot$. For this geometry, which corresponds to the model result at 12:18 UT discussed below, an exactly Earth-directed CME

would have a nearly round halo ($31.4/28.2 \simeq 1.1$), as is commonly observed.

3.2. *Model-Data Comparisons: The Near-Sun Region*

In order to compare the model flux rope to the observed halo, we use the results of the model calculation, apex height Z and apex width $4a$, along with the specified flux rope ellipse eccentricity ϵ, to construct a three-dimensional representation of the flux rope. This three-dimensional structure can then be oriented in space in order to provide model morphological results for comparison to the CME image data. The geometry used in this case is illustrated in Figure 7. Here $Z \simeq 2R_1$, where Z is slightly smaller because the sunward end of the flux rope ellipse lies slightly inside the photosphere (the flux rope has footpoints embedded in the photosphere at fixed locations). The three-dimensional flux rope geometry is constructed by computing the positions of a large number of points that outline the flux rope's exterior surface. In order to determine the shape of the halo, only the exterior positions are needed; to compute synthetic coronagraphs, interior points and density values must also be computed.

For the purpose of orienting the three-dimensional flux rope geometry, we define a coordinate system with its origin at Sun center, the z-axis upward, the x-axis directed toward the west limb, and the y-axis directed along the Earth-Sun line, away from Earth. When orienting the flux rope, we include five angles: source latitude (λ_0), source longitude (ϕ_0), a tilt in the direction of latitude (α_x), a tilt about the direction of motion of the flux rope apex (α_y), and a tilt in the direction of longitude (α_z).

It is easy to see that the final position of the flux rope is dependent on the order in which the various tilts are applied. For this reason, a detailed procedure must be provided. To orient the model flux rope for comparison to the data, we begin with the flux rope ellipse in the plane of the ecliptic, situated so that one end of the major axis of the ellipse (the "footpoints") sits at Sun center. Initially, the flux rope extends outward in the negative y-direction, as would be the case for a front-side halo CME. This is illustrated in Figure 8*a*, where a plot indicating the outer surface of the model flux rope is shown with all angles set equal to zero. Here points arrayed coarsely across the flux rope surface are projected into the plane of the sky; the Sun is indicated by a small circle in the center of each plot.

We first apply the tilt angle α_y (a rotation about the y-axis). This is illustrated in Figure 8*b*, where the tilt is $\alpha_y = 75^\circ$, corresponding to a clockwise rotation. We next apply the latitude tilt angle α_x (a rotation about the x-axis). This is illustrated in Figure 8*c*, where $\alpha_x = 24^\circ$, corresponding to a tilt toward higher latitude. Longitude tilt angle α_z (a rotation about the z-axis) is next; this is shown in Figure 8*d*, where $\alpha_z = 11^\circ$, corresponding to a tilt toward the solar west limb. After the directional angles are applied, we translate the geometry by $-R_\odot$ in the y-direction, moving the footpoints outward to the solar surface at disk center. We then move the source location to the correct latitude λ_0 (another rotation about x). This is illustrated in Figure 8*e*, where $\lambda_0 = -22^\circ$. Finally, the source location is moved to the correct longitude ϕ_0 (another rotation about z; see Fig. 8*f*). To provide additional examples, we note that angles $\alpha_x = \alpha_y = \alpha_z = 0^\circ$, $\lambda_0 = 0^\circ$, and $\phi_0 = 90^\circ$ correspond to a west-limb event at the solar equator, viewed exactly axially, as in Figure 7*a*, and $\alpha_x = \alpha_z = 0^\circ$, $\alpha_y = \pm 90^\circ$, $\lambda_0 = 0^\circ$, and $\phi_0 = 90^\circ$ correspond to Figure 7*b*. As discussed above, the source location in this case is at latitude $\lambda_0 = -22^\circ$ and longitude $\phi_0 = -10^\circ$.

Figure 2 shows model-data comparisons corresponding to each of the LASCO images that were measured as indicated in Figure 1 for the 12:18 UT image. Here the orientation angles are set at fixed values, chosen to provide a best fit to all four coronagraph images for this event. Specifically, after each run of the model, the orientation angles were adjusted, by trial and error, to obtain the best fit, on average, to the measured halo points. For this study, the ambient coronal and solar wind parameters were assumed to be functions only of the flux rope apex height above the photosphere (Z). Under this assumption, the computed flux rope dynamics are independent of the orientation angles (that is, the orientation angles can be adjusted without recomputing the model dynamics). In all cases, the model parameters were adjusted to obtain approximate agreement with the halo dynamics in the near-Sun region while maintaining agreement with the Sun-Earth ICME transit time and the flux rope field amplitude at 1 AU. Because the dynamics can be computed quickly (a matter of minutes on a typical personal computer), numerous runs were performed.

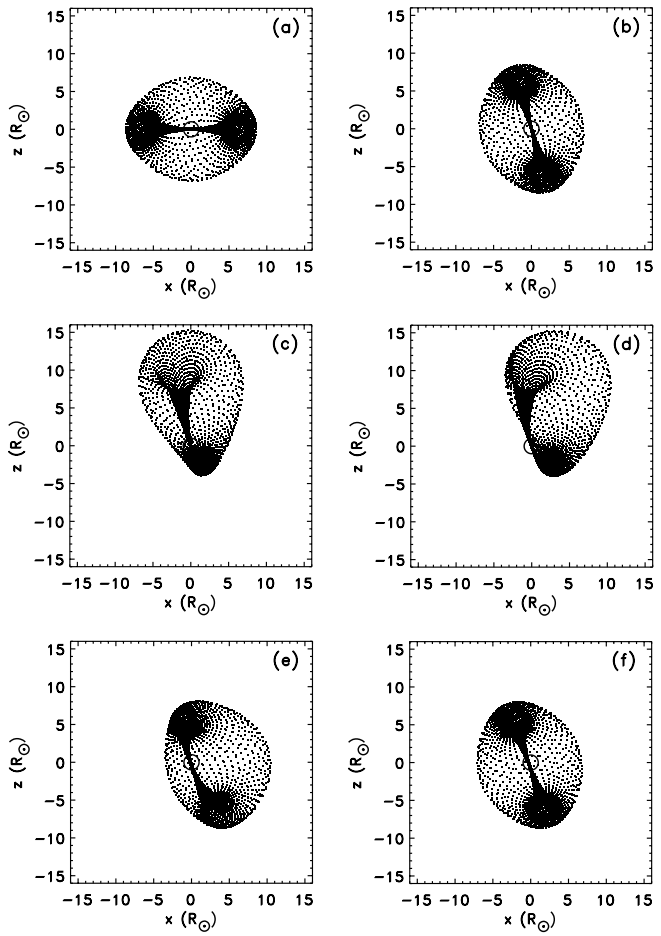

FIG. 8.—Plots projecting the shape of the outer surface of the model flux rope onto the plane of the sky, with various orientation angles: (*a*) all angles set equal to zero; (*b*) same as (*a*), but with $\alpha_y = 75^\circ$; (*c*) same as (*b*), but with $\alpha_x = 24^\circ$; (*d*) same as (*c*), but with $\alpha_z = 11^\circ$; (*e*) same as (*d*), but with $\lambda_0 = -22^\circ$; (*f*) same as (*e*), but with $\phi_0 = -10^\circ$. Flux rope parameters correspond to time 11:42 UT.

In each panel of Figure 2, the outline of the projected model-CME halo is indicated by the open circles. For example, the outline of the model flux rope of Figure 8*f* corresponds to that shown at 11:42 UT in Figure 2. As discussed above, the filled squares in Figure 2 correspond to positions measured in the coronagraph images. Note that while the orientation of the actual CME is changing slowly (see § 2 and Fig. 3), the orientation of the model flux rope is fixed. In this case, we adjusted the orientation angles, particularly the tilt angle α_y, to obtain the best fit

for the outermost C3 images. We shall see that this choice of α_y, which results in the flux rope axis (the direction of the observed halo elongation) aligned mostly north-south, also yields the correct orientation for the model ICME fields at 1 AU.

We see that the model and the data match quite well, with the exception of the measured halo at 11:30 UT. In that case, the measured halo (*filled squares*) is clearly tilted relative to the model halo (*open circles*). This is quantified in Figure 3, where the eccentricity and tilt angle of the model halo ellipse are plotted as curves in the top and bottom panels, respectively. Here the model halo is analyzed at each time step by fitting an ellipse to the model halo points (e.g., Fig. 2, *open circles*). As discussed above, the filled squares in Figure 3 are obtained by similarly fitting an ellipse to the observed halo points for each coronagraph image. In addition, as discussed above, the tilt angle increases in the clockwise direction relative to the solar equator. For the special case in which $\alpha_x = \alpha_z = \lambda_0 = \phi_0 = 0^\circ$, this tilt angle is equal to α_y.

Clearly, the actual flux rope that underlies this CME event is evolving in terms of its orientation. Given that deflections in the direction of motion for CMEs are common (see, e.g., Table 2 of Krall et al. 2001), it is not surprising that the tilt of the flux rope axis should evolve as well. Using the neutral line and the postflare loops as indicators of the initial orientation of the flux rope axis, as was done with the neutral line in Chen et al. (2000), we observe an initial tilt of approximately 35°. This, combined with the increase in the observed halo ellipse tilt angle from 43° at 11:30 UT to 65° at 12:42 UT, indicates a smooth evolution of the orientation of the flux rope that underlies the CME. Our simple model CME, by contrast, has fixed orientation angles, which best fit the observed halo ellipse tilt angle at 12:42 UT. These orientation angles are $\alpha_x = 24^\circ$, $\alpha_y = 75^\circ$, and $\alpha_z = 11^\circ$ (see Fig. 8). Thus, with the flux rope interpretation in mind, the measurements indicate a change in the orientation of the flux rope axis from 35°, as indicated by the postflare loops, to a tilt angle $\simeq \alpha_y = 75^\circ$, as indicated by the model-data match at 12:42 UT.

Because the model uses fixed orientation angles, the agreement in this respect varies. For the angles used here, the agreement is quite good for the C3 data and less so for the C2 data. The model-data match at 11:30 UT is further degraded by the details of the dynamics. Specifically, the flux rope tends to "pinch" early in the eruption, when the magnetic helicity is being increased (see § 3.5). The result is a narrower flux rope and a more elongated halo. This effect is visible in Figure 2 (11:30 UT) and Figure 3 (*top*).

Our assertion that the CME halo is elongated along the direction of the underlying flux rope axis is further supported by generating a synthetic coronagraph for this event, shown in Figure 9. This figure shows a faint CME "halo" with size and orientation similar to that of Figure 1. Figure 9 also shows prominent round features, situated north-northeast and south-southwest of the occulting disk, which correspond to the legs of the flux rope. Figure 1 shows a similar round feature, which apparently corresponds to the south-southwest feature of Figure 9. Figure 1 also shows a very faint north-northwest looplike feature that may correspond to the other leg of the underlying flux rope. In Figure 1, the south-southwest looplike feature is less saturated than the corresponding feature in the synthetic image and further shows a number of details, including that it is somewhat hollow. In fact, the legs in the model flux rope are similarly hollow, but this is not evident because the synthetic image has been saturated so as to make the faint halo visible. An inset image in Figure 9 shows the south-southwest leg with much less image saturation. In the inset, the density structure in the leg is visible. (Its appearance is similar to an axial view of a flux rope CME near the limb and is also similar to the south-southwest feature of Fig. 1.)

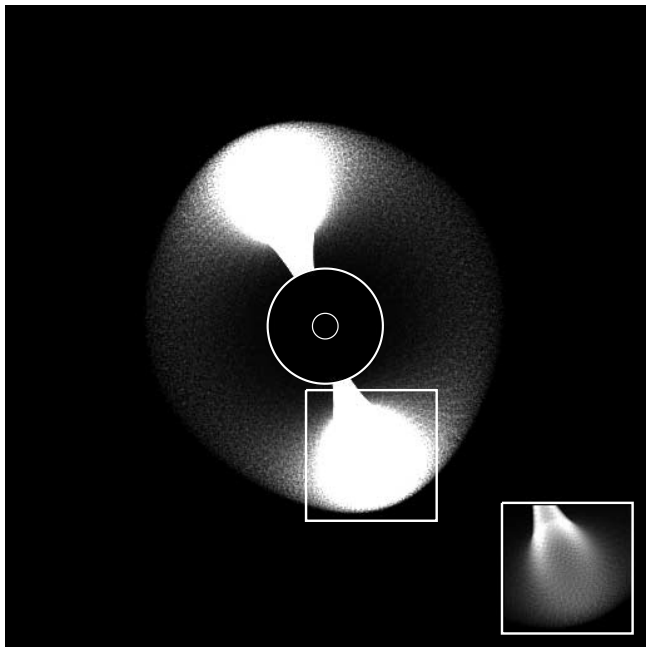

FIG. 9.—Synthetic coronagraph image of the model flux rope CME at 12:18 UT. The inset image in shows the south-southwest round feature with less image saturation.

In generating the synthetic coronagraph image of Figure 9, we have made a number of assumptions. First, we assume that the center-to-edge density profile is related to that of a model preeruption flux rope (Krall & Chen 2005). This was determined in this case by using equation (11) of Krall & Chen (2005), with field profiles corresponding to those used in Figure 5 of that paper and coefficients $\bar{B}_t$ and B_p adjusted to approximate the initial model field values used in the present model event. In order to relate the CME density structure to the preeruption density structure we further assume that once the velocity of the apex of the erupting flux rope exceeds the sound speed of the plasma within the flux rope, plasma does not flow along its length (early in the eruption, however, plasma is assumed to flow freely; see § 2.2 of Krall et al. 2000 for a discussion of this). Thus, the CME density is computed by applying simple expansion factors to the preeruption density, with adjustments made to account for the assumed flow of plasma within the flux rope early in the eruption.

Thus, gravity has not been included for the purpose of draining this plasma from the legs of the flux rope. We believe this to be an unrealistic aspect of the model with respect to the plasma within the legs of the flux rope and further believe that this accounts for the fact that the legs of the model flux rope, as shown in Figure 9, are much more prominent than the legs in the corresponding LASCO C3 image (Fig. 1). Note that in the EFR model, the forces and the resulting motions are computed only for the apex of the flux rope (the rest of the flux rope is assumed to expand outward as dictated by the apex motion). Thus, model results are not sensitive to the density structure within the legs of the flux rope. Note also that the physical effect of gravity acting on the prominence mass within the flux rope, which is distinct from the plasma that makes up the bright rim of the CME, is included. In the model, prominence matter drains out of the flux rope to a specified degree over a specified timescale (Chen 1996; Krall et al. 2000).

3.3. *Model-Data Comparisons: The Near-Earth Region*

For the EFR model, model-data comparisons in the near-Earth region can be accomplished by evolving the model flux rope beyond $Z > 1$ AU and by applying the orientation angles as in the near-Sun comparison. Equivalent in situ curves are then generated by diagnosing the position of Earth within the model flux rope and determining the model field, density, velocity, etc., at that point. In order to obtain the ICME field, the handedness of the flux rope and the sign of the leading-edge field must be specified (model dynamical results are independent of these two quantities). These selections can be guided by observation by assuming, as is done in the model (see Fig. 1 of Krall et al. 2000), that the leading-edge field has the same sign as the active region field above the neutral line and by further assuming that the handedness of the ICME is the same as that of the preeruption arcade. It has been shown that these are valid assumptions in this case (Yurchyshyn et al. 2005).

Figure 6 shows a model-data comparison at 1 AU for this event. The solid curves are *ACE* data; note that there was a data dropout in the proton density from October 29 06:20 UT to October 30 04:22 UT. The model results (*dashed curves*) provide a good match to the overall timing (the arrival time agrees to within 1 hr) and to the various field components. In order to obtain this model-data match, one of the flux rope orientation angles, α_z, was increased from 11°, the value used to obtain the model results of Figures 2, 3, and 9, to 18°, corresponding to a 7° deflection (rotation) toward the solar west limb, relative to the Earth-Sun line. As in the near-Sun case, the determination of the deflection was accomplished by trial and error. Note that all other flux rope orientation angles (source location angles λ_0 and ϕ_0 and tilt angles α_x and α_y) and all model inputs have been held constant.

With $\alpha_z = 18°$, the axis of the model flux rope comes within $\simeq$0.12 AU of the *ACE* spacecraft. At the time of closest approach ($\simeq$17:00 UT) the overall width of the model ICME is $4a \simeq 0.76$ AU, where the width of the current channel within the flux rope is $2a \simeq 0.38$ AU. It is within the current channel that the field direction rotates smoothly as in a magnetic cloud.

While Figure 6 shows that the data and the model match quite well, we note that there is a great deal of structure near the front of the actual ICME that is not present in the simple model. In addition, the model velocities appear to be about 30% too small, even though the transit time is correct to within 1 hr. Because the interplanetary dynamics are so ill-understood at present, it is possible that the actual interplanetary forces differ greatly enough from the model to routinely produce a higher velocity (relative to the model), with the same transit time, for ICMEs that are fast in comparison to the solar wind. This would indicate a near-Sun deceleration that is stronger than in the model, followed by a near-Earth deceleration that is weaker than in the model. In this case, however, the ICME was shortly followed by another high-speed ICME with virtually no gap between the two being recorded at the *ACE* spacecraft (Skoug et al. 2004). Thus, it is entirely possible that a shock driven by the subsequent ICME, or even the subsequent ICME itself, drove the ICME shown in Figure 6 to a higher velocity than it might have had if it were an isolated event, as in the model. The solar wind velocity is significant because stronger velocities tend to cause greater compression of the magnetosphere leading, for example, to a stronger cross polar potential.

Hu et al. (2005) have analyzed the *ACE* data for this event by performing a Grad-Shafranov reconstruction of its magnetic structure. Their analysis finds a peak field of 47 nT, with the *ACE* spacecraft coming within 0.09 AU of the magnetic axis of the reconstructed flux rope. We note that in the EFR model, neither the flux rope cross section nor the flux rope field structure are allowed to distort, as expected from past simulations (Cargill et al. 1995; Riley et al. 2003; Manchester et al. 2004) and as indicated by observations for this event (Hu et al. 2005) and others (Riley et al. 2003). Thus, in obtaining a good match to the observed fields, we find a larger peak magnetic field of 79 nT. Given the simplifying assumptions of the model and the fact that the result of Hu et al. (2005) is based on single-spacecraft data, we feel that both results are uncertain to a degree at which we find no significant disagreement between the data and the model.

Finally, we note that the analysis of Hu et al. (2005) indicates that the axis of the flux rope is inclined by 86° from the horizontal coordinate (y) in the geocentric solar ecliptic (GSE) coordinate system (Kivelson & Russell 1995). This compares well with the model tilt angle $\alpha_y = 75°$ and is qualitatively consistent with the slow rotation of the flux rope axis that is implied by observations at the solar surface (the orientation of the postflare arcade; see Fig. 5) and in the near-Sun region (the direction of halo elongation; see Fig. 3). For further discussion of the field orientation at the source and at 1 AU for this event, see Yurchyshyn et al. (2005).

3.4. *Model-Data Comparisons: The Computed Magnetospheric Response*

We now consider the computed magnetospheric response to the model solar wind of Figure 6. Here we use the time-dependent, global, three-dimensional MHD magnetospheric simulation model of Lyon et al. (2004). The LFM model has been employed by numerous researchers for S3C event studies (Fedder et al. 1997; Slinker et al. 1998, 1999), studies of ICME-magnetosphere interactions (Chen et al. 1995), and studies of magnetosphere-ionosphere coupling (Sojka et al. 1997, 1998; Wiltberger et al. 2004). It is a central component of the Center for Integrated Space Weather Modeling (CISM) effort (Goodrich et al. 2004; Wang et al. 2004).

In order to use the solar wind data (Fig. 6) to drive the LFM model, we first convert from GSE coordinates to solar magnetic (SM) coordinates, which have axes parallel to the Earth-Sun line and to Earth's dipole (Kivelson & Russell 1995). As an example, the components of the solar wind field, B_y and B_z, are shown in Figure 10. Here the *ACE* data are shown as a solid curve and the model result as a dotted curve. Additional solar wind inputs include the proton density, temperature, and velocity vector. At times when there were dropouts in the *ACE* density data (see Fig. 6, *second panel*), values were filled in using the model result.

These two sets of solar wind inputs (data and model) were used to drive two separate runs of the LFM model. Model magnetospheric responses to the two sets of solar wind inputs are also shown in Figure 10 (*bottom*). Plotted are the cross polar potential for the North Pole (*bottom left*) and the North polar upward field-aligned current (*bottom right*).

We see that the two responses deviate significantly during the first 8 hr of the event, at which time the measured solar wind shows evidence of one or more IP shocks. Thereafter, the potential and current curves agree rather well, although the model-driven curve leads the data-driven curve by about 2 hr. Note that this timing mismatch can be partially attributed to the mismatch in the model ICME arrival time (Fig. 6, *top*). In any case, the phase shift between the model-driven curves and the data-driven curves (Fig. 10, *bottom*) is clearly related to the phase shift between the

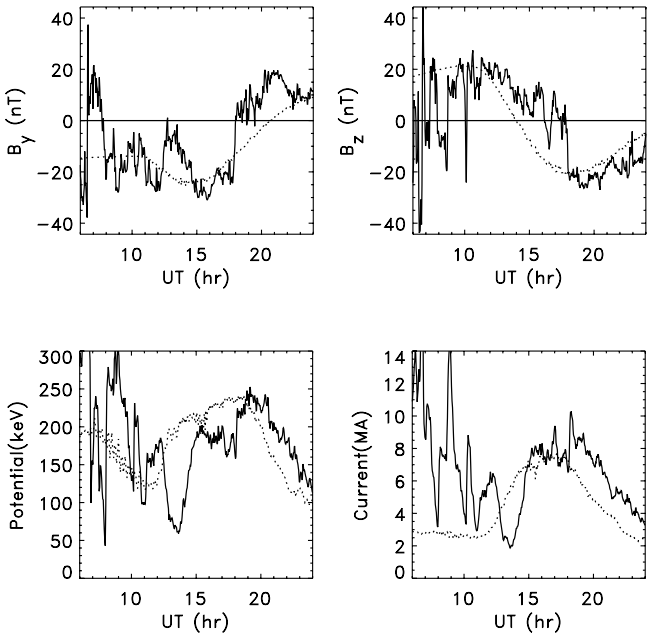

FIG. 10.—*Top:* Solar wind magnetic field data for 2003 October 29. Overlaid on the data are corresponding field components (*dotted curves*) for the model ICME. *Bottom:* Magnetospheric response to the solar wind inputs: the North Pole cross polar potential (*left*) and the North polar upward field-aligned current (*right*). Solid curves are the response to the actual solar wind input; dotted curves are the response to the model solar wind.

two B_z curves (Fig. 10, *top right*). The effect of the solar wind velocity, which is greater than the model velocity throughout, is less clear. It would be interesting to perform a series of simulations in order to isolate these effects. For example, one might selectively introduce the model fields, densities, and velocities into an otherwise data-driven LFM simulation. This, however, is beyond the scope of the work we report here.

Figure 11 shows computed power input into the ionosphere from resistive heating (*top*) and electron precipitation (*middle*). The total power is also shown (*bottom*). In each plot, the solid curve is the LFM result as driven by the actual solar wind data, and the dotted curve is that driven by the model solar wind input. Because a significant fraction of the energy entering Earth's environment from the solar wind is deposited in the polar caps via Joule heating and energetic particle precipitation, these curves represent key magnetospheric responses to the solar wind. As with the cross polar potential and field-aligned current (Fig. 10 *bottom*), the model-driven and data-driven results are, overall, in only qualitative agreement. Late in the simulation period, however, the degree to which the model-driven response tracks the data-driven response is remarkable. Furthermore, the total energy deposition (integrated total power) for the two cases agrees to within 23%.

3.5. *Best-Fit Model Parameters*

In order to perform the calculations of the EFR model, flux rope initial conditions must be specified, along with helicity inputs (which drive the eruption). Ambient field and plasma conditions, which affect the motion of the flux rope, must also be specified. In this model, the flux rope begins with its apex at a specified height, which we take to be $Z_0 = 100$ Mm, with a specified separation between the stationary flux rope footpoints. We note that the irregular shape of the neutral line suggests a magnetic geometry that is more complicated than that of our simple model (see, e.g., Figs. 1 and 4*a* of Chen et al. 2000).

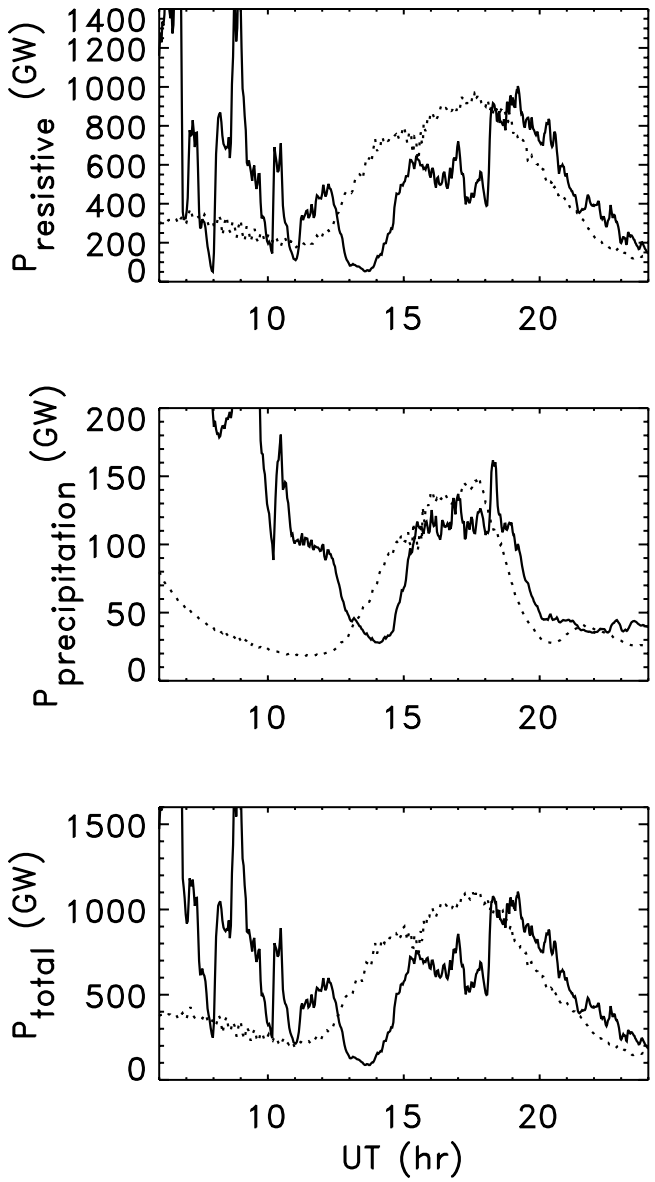

FIG. 11.—Computed power input into the ionosphere from resistive heating (*top*) and electron precipitation (*middle*). The total power is also shown (*bottom*). In each plot, the solid curve is the LFM model response to the solar wind data input, and the dotted curve is the response to the model solar wind input.

Nevertheless, we use the overall length of the active region as a proxy for the separation between the flux rope footpoints, which is one of our model inputs. Thus, we use a footpoint separation distance of $S_f = 300$ Mm $\simeq 0.43\ R_\odot$ in our model calculations. Because the coronagraph observations for this event do not resolve the main acceleration phase for this event, and because the main-phase acceleration profile is the aspect of an erupting flux rope that is most sensitive to the footpoint separation distance (Chen & Krall 2003), our ability to obtain a match between the model results and the observations was not strongly affected by our choice of S_f.

Along with Z_0 and S_f, we specify the ratio of the initial current-channel radius to the initial radius of curvature at the apex, $1/a_0\kappa_0 = 2$, the initial flux rope density, $n_0 = 1.3 \times 10^8$ cm^{-3}, the initial fraction of the mass that is represented by prominence material, 0.5, and the initial temperature, 2×10^6 K. Because the active region at the source of the eruption is rather strong, we

specified a background field $B_{c,0} = 15$ G, which is larger than the usual values of the order of 1 G; this field is specified to peak at a height of 110 Mm. We also specify the plasma density versus height, covering both the solar corona and the solar wind. This function is the same as that used in Krall et al. (2000) and gives an ambient density of $n_c \simeq 2.4 \times 10^8$ cm^{-3} at height Z_0. Based on these inputs and on the assumption that the flux rope begins in an equilibrium state, the initial model flux rope has an average toroidal (axial) field of $\bar{B}_{t,0} \simeq 3.2$ G, a characteristic poloidal (twist) field of $B_{p,0} \simeq 3.2$ G, and current-channel radius of $a_0 \simeq 81$ Mm.

To drive the flux rope out of equilibrium, an increase in the flux rope helicity is specified, which, in this case, increases the poloidal flux from its initial value of 1.5×10^{22} G cm^2 to a final value of 7.4×10^{22} G cm^2. This occurs very rapidly, over a period of 18 minutes. The interpretation of this helicity increase has been discussed at length elsewhere (Krall et al. 2001; Chen & Krall 2003). Here we say only that the origin of the helicity increase is not specified in the model and that it might be due to either macroscopic reconnection, as in the arcade–to–flux rope models (Mikić & Linker 1994; Antiochos et al. 1999; Chen & Shibata 2000; Amari et al. 2000; Linker et al. 2001; Cheng et al. 2003), or to an unknown subphotospheric process that drives current along the length of the flux rope (Chen 1996). In this case, the initial energy associated with the toroidal field is 3.2×10^{32} ergs, the initial energy associated with the poloidal field is 9.7×10^{32} ergs, and the additional helicity corresponds to an addition of 2.0×10^{33} ergs to the flux rope magnetic energy budget. Note that the fluxes in our case, toroidal flux of 6.6×10^{20} G cm^2 and poloidal flux of 7.4×10^{22} G cm^2, are comparable to the axial flux computed by Hu et al. (2005) from their reconstruction of the ICME fields, 5.4×10^{21} G cm^2.

As discussed in § 3.1, we assume that as the flux rope expands outward from the Sun its axis is shaped like an ellipse, with the ellipse eccentricity being a model input. Because we are fitting a three-dimensional object (a flux rope) to a set of two-dimensional data (coronagraph images), the eccentricity of the flux rope ellipse is not uniquely determined. While we show results for $\epsilon = 0.78$, we were also able to obtain good matches to the data for $\epsilon = 0.70$ and 0.83. In these cases we adjusted other parameters to compensate. Relative to the $\epsilon = 0.78$ case, the flux rope was adjusted to have a larger (smaller) apex width for a smaller (larger) value of ϵ. Further discussion of the treatment of the flux rope ellipse in the model appears in the Appendix.

As the flux rope expands it also cools, based on a specified polytropic index $\gamma = 1.1$, which, based on previous studies, is a typical value. Furthermore, a fraction of the flux rope mass is allowed to "drain out," representing the loss of 85% of the prominence material; the posteruption mass in the flux rope is $\simeq 2.0 \times 10^{15}$ g.

As the flux rope moves outward, it interacts with the solar wind through a drag coefficient c_d. We note that we have updated the drag term relative to our previous treatments to better represent our current understanding of flux rope CME geometry. Thus, our value of $c_d = 0.27$ is not simply related to the values used in past studies (see the Appendix for a discussion of this). Based on the preevent solar wind speed, we specify an asymptotic solar wind speed of 600 km s^{-1}. Here the solar wind begins at a height of 200 Mm, reaching full speed at a height of 10 $R_\odot$. We note that the physics in the interplanetary medium is far from well known. In our case, we compute a simple momentum transfer from the flux rope to the solar wind particles. However, if the flow around the flux rope is laminar, some of that momentum is recovered, and c_d should be reduced. Conversely, if the solar wind is magnetized with field lines perpendicular to the both the motion of the flux rope apex and the alignment of the flux rope axis, then magnetized solar wind plasma might be dragged along, and c_d should be increased. We are hopeful that further modeling of CME/ICME events will provide useful guidance on this subject. For this study, c_d was treated as a free parameter, such that both c_d and the flux rope field could be increased or decreased (the flux rope field is adjusted by adjusting B_c) while preserving the value of the Sun-Earth transit time.

In summary, observations are used to set the asymptotic model solar wind speed and to guide the selection of the footpoint separation S_f. Source location angles λ_0 and ϕ_0 are also determined from observations but are applied after the model dynamics have been computed in order, for example, to generate synthetic coronagraphs. Similarly, the sign and the handedness of the flux rope field can be guided by the observations (see § 3.3) but are not specified as model inputs. In the present study they are specified after the fact in order to obtain ICME fields. Other model inputs, to which the results are less sensitive, are set to usual values. These include the initial height Z_0, the initial temperature, the polytropic index γ, parameters affecting the evolving mass of prominence material within the flux rope, parameters affecting the shape of the solar wind velocity profile, and the ambient coronal and solar wind density function. The remaining parameters are adjusted to obtain the appropriate dynamics for the event. We adjust $1/a_0\kappa_0$ to vary the thickness of the flux rope. Flux-rope eccentricity ϵ is chosen to control the length of the projected model "halo" relative to its width. The initial density n_0 is used to vary the density at 1 AU; it also affects the interplanetary dynamics through the flux rope inertia. The ambient field B_c affects the initial equilibrium flux rope field; in combination with the helicity injection function, it determines the outward force on the flux rope and, consequently, the strength of the magnetic field at 1 AU. As discussed above, the outward force is countered by a drag force, which is adjusted via a drag coefficient, c_d. In practice, the overall model-data match is iterated by alternating between improving the near-Sun and near-Earth matches.

4. DISCUSSION

We have shown that the EFR model (Chen & Garren 1993; Chen 1996; Krall et al. 2000), with appropriate modifications (see the Appendix) can reproduce both quantitative near-Sun properties of the 2003 October 28 coronal mass ejection and the timing, strength, and orientation of the fields measured in situ at 1 AU. This is accomplished via a one-dimensional, time-dependent model calculation of a three-dimensional object moving through a one-dimensional model corona and solar wind. With the calculation complete, the orientation of the flux rope (direction of propagation plus a tilt around that direction) is determined in order to match the shape and morphology of the CME halo, as observed in the near-Sun coronagraph images. The orientation of the flux rope is separately determined at 1 AU. For this event, only one of the orientation angles differed between the near-Sun and near-Earth matched results, corresponding to a deflection of 7° toward the solar west limb, relative to the Earth-Sun line. In producing the near-Sun match, we have shown that the direction in which the CME halo is elongated corresponds to the projected orientation of the flux rope axis.

The morphological halo and leg features in the LASCO C2 and C3 images (see Fig. 1) and the presence of similar features in model-based synthetic coronagraph images (see Fig. 9) support

this correspondence between the halo elongation and the magnetic axis of the flux rope. Here the EFR model reproduces the observed morphology if the axis of the flux rope in the near-Sun region—the region observed by LASCO—is approximated to be an ellipse with one end attached to the photosphere and with an eccentricity in the range $0.70 < \epsilon < 0.83$ (see Fig. 7).

Based on the orientation of the posteruption arcade, which is believed to be aligned with the flux rope axis (Yurchyshyn et al. 2005), on the evolving orientation of the CME halo, which we show is elongated in the direction of the flux rope axis, and on analysis of the ICME fields by Hu et al. (2005), we conclude that the orientation of the magnetic axis of the flux rope in this event rotated smoothly through approximately 50° as the flux rope apex expanded from the solar surface to 1 AU. This can be seen in Figure 5, which shows posteruption loops aligned along a neutral line (see also Fig. 4) with tilt angle $\simeq$35°, in the tilt of the observed halo, increasing smoothly from 43° to 70° (see Fig. 3), and in Hu et al. (2005), in which a tilt angle of 86° is determined from the ICME measurements. Furthermore, we find that most of the rotation occurs in the near-Sun region. Thus, the degree to which the model flux rope was tilted out of the plane of the ecliptic, which was determined by matching the model to the data in the near-Sun region, resulted in an ICME with an approximately correct tilt at 1 AU. We believe this to be the best demonstration of CME/ICME correspondence to date.

Finally, using the LFM global magnetospheric simulation code, we find that our model solar wind properties at 1 AU produce a magnetospheric response in qualitative agreement with that computed using the actual solar wind data. With respect to the total energy deposition into the polar cap ionosphere, the model-driven and data-driven LFM simulations agree to within 23%.

This work was supported by NASA (DPR W-10106 and W-10233, LWS TRT program) and the Office of Naval Research. V. Y. was supported, in part, by NSF grant ATM 05-36921, NASA grant NAG5-9682, and NASA ACE NNG0-4GJ51G. Work at Los Alamos was performed under the auspices of the US Department of Energy, with financial support from the NASA ACE program. J. Krall wishes to thank A. A. van Ballegooijen of the Harvard-Smithsonian Center for Astrophysics for a helpful discussion of flux rope orientation angles.

APPENDIX

AN UPDATED FLUX-ROPE MODEL FOR HALO-CME EVENTS

As discussed in § 3, we find that the assumption made in previous event studies (Chen et al. 1997, 2000; Wood et al. 1999; Krall et al. 2001), that the flux rope is represented by a section of a torus in which the axis of the flux rope has a circular shape, does not provide a good match to the halo CME event in this study. Thus, we have modified the erupting flux rope (EFR) model (Chen 1996; Krall et al. 2000) to allow for an elliptical shape after eruption.

Furthermore, as a result of our past studies, we have determined that the width of the apex of our model flux rope is $4a$, so the leading edge lies at height $Z + 2a$, where Z is the distance from the photospheric source to the magnetic axis of the flux rope at its apex and a is the radius of the current channel within the flux rope. For the purpose of computing the drag force acting on the flux rope apex as it pushes (or is pushed by) the solar wind, this geometry contradicts that assumed in Chen (1996) and Krall et al. (2000).

In this appendix, we describe the EFR model equations that were updated for this study. In so doing, we include equations that were updated relative to those given in Krall et al. (2000).

A1. AN ELLIPTICAL FLUX ROPE

In the EFR model, we compute the motion of the apex of a flux rope that has footpoints rooted in the photosphere. The flux rope is described by apex height above the photosphere, Z, and the current-channel radius at the apex, a. Following Garren & Chen (1994), we use the local radius of curvature κ to compute the curvature force at the apex of the flux rope, so that

$$\mathcal{M}\frac{d^2Z}{dt^2} = \frac{I_t^2\kappa}{c^2}\left[\ln\left(\frac{8}{a\kappa}\right) - 1 + \frac{\xi_i}{2} + \frac{1}{2}\beta_p - \frac{1}{2}\frac{\bar{B}_t^2}{B_{pa}^2} - \frac{2}{a\kappa}\frac{B_{\perp c}}{B_{pa}}\right] + F_g + F_d, \tag{A1}$$

where $\mathcal{M}$ is the mass per unit length at the apex of the flux rope, including bright rim plasma and prominence mass, I_t is the toroidal current, ξ_i is the internal inductance, the value of which is dependent on the specific choice of current profile versus minor radial coordinate r, $\bar{B}_t$ is the average toroidal (axial) field within the flux rope current channel ($r \leq a$), B_{pa} is the poloidal (twist) field amplitude at $r = a$, $B_{\perp c}$ is the component of the ambient coronal magnetic field that is perpendicular to both the direction of motion of the apex and the flux rope axis at the apex, F_g is the force due to gravity, and F_d is the drag force, which results from the interaction of the flux rope with the solar wind plasma.

In equation (A1),

$$\beta_p = \frac{8\pi(p_i - p_c)}{B_{pa}^2}, \tag{A2}$$

where p_i is the pressure inside the flux rope and p_c is the ambient pressure. In short, equation (A1) is simply equation (2) of Krall et al. (2000), but with R (the "major radius") replaced by $1/\kappa$.

In addition to changing the form of the outward $\boldsymbol{J}\times\boldsymbol{B}$ force in equation (A1), the elliptical shape of the flux rope also changes the inductance. Whereas before the circular shape allowed simplification of the expression for the inductance (see Landau & Lifshitz 1960, p. 138), the elliptical shape does not. Thus,

$$L = \frac{1}{c^2}\int_{\theta_f-\pi/2}^{\pi/2} ds \int_{s+\psi_0}^{s+2\pi-\psi_0} d\psi \, \frac{R_1^2 \cos s \cos\psi + R_2^2 \sin s \sin\psi}{\left[R_1^2(\sin s - \sin\psi)^2 + R_2^2(\cos s - \cos\psi)^2\right]^{1/2}}, \tag{A3}$$

where θ_f is the angle between the downward vertical and one of the ellipse footpoints, s and ψ are polar coordinate angles in a coordinate system that is centered at the center of the ellipse, R_1 is one-half the length of the ellipse major axis, R_2 is one-half the length of the ellipse minor axis, the integral over ψ is limited to values that correspond to points above the photosphere, and $\psi_0(s) \simeq a(s)/2(R_1^2\cos^2 s + R_2^2 \sin^2 s)$.

As before, the fields and the toroidal (axial) current are calculated from the toroidal and poloidal fluxes. Note that the inductance enters into the calculation of the poloidal (twist) field and therefore affects the minor radial forces that are computed to determine $a(t)$ (see eq. [8] of Krall et al. 2000).

Note also that the geometry of the flux rope ellipse enters into the equations in a number of other ways. These include the relationships between ϵ, Z, the footpoint separation S_f, and the flux rope ellipse axes lengths R_1 and R_2, the curvature at the apex $\kappa = R_1/R_2^2$, the fraction of the flux rope that is above the photosphere (Θ in Chen 1996; Krall et al. 2000), and the flux rope volume.

A2. NEAR-SURFACE FLUX ROPE GEOMETRY

In Chen & Krall (2003) it was found that the main acceleration phase of an erupting flux rope is related to its geometry because for a circular flux rope the radius of curvature is minimum, and the geometrical factors in the $\boldsymbol{J}\times\boldsymbol{B}$ force are therefore maximum when the flux rope is semicircular, $Z = Z_* = S_f/2$.

Because we believe the circular approximation is valid near the solar surface, we begin with eccentricity $\epsilon = 0$ and increase this in an ad hoc way, as a function of height, to obtain the specified value ($\epsilon = 0.78$ in this case). In this case, we begin to deviate from the circular approximation at height $Z = R_\odot$, reaching the asymptotic value of 0.78 at $Z = 8\ R_\odot$. We find that the results are not sensitive to the specified height range over which the flux rope evolves from circular to elliptical.

A3. INTERPLANETARY DRAG FORCES

In previous model calculations, the interaction between the flux rope motion and that of the background solar wind was accounted for via a simple drag force, $F_d = -c_d n_c m_p a(V - V_c)|V - V_c|$, where c_d is a dimensionless drag coefficient, n_c is the ambient coronal proton number density, m_p is the proton mass, $V = dZ/dt$, and V_c is the Z-component of the solar wind velocity. This expression, which was formulated before the model was first compared to coronagraph data by Chen et al. (1997), describes an object with a circular cross section of radius a, moving through a medium of density $m_p n_c$ with relative velocity $V - V_c$. For $V > V_c$ the flux rope is assumed to be imparting kinetic energy to the solar wind protons as it displaces those protons from its path (for $V < V_c$, the opposite occurs).

However, as a result of numerous model-data comparisons (Chen 1996; Wood et al. 1999; Chen et al. 2000; Krall et al. 2001), we have determined that the effective radius of the flux rope cross section at its apex is not a but $2a$. Furthermore, the expansion of this width is large enough that the leading-edge velocity $V_{\rm LE} = V + 2V_a$, where $V_a = da/dt$, differs significantly from V. Thus, the flux rope is either pushing into the solar wind with relative velocity $V + 2V_a - V_c$ or being pushed by the solar wind with relative velocity $V_c - V + 2V_a$. We therefore use

$$F_d = \begin{cases} -2c_d n_c m_p a(V + 2V_a - V_c)^2, & V \geq V_c, \\ 2c_d n_c m_p a(V_c - V + 2V_a)^2, & V < V_c. \end{cases} \tag{A4}$$

REFERENCES

Amari, T., Luciani, J. F., Mikić, Z., & Linker, J. 2000, ApJ, 529, L49
Antiochos, S. K., DeVore, C. R., & Klimchuck, J. A. 1999, ApJ, 510, 485
Bieber, J. W., Clem, J., Evenson, P., Pyle, R., Ruffolo, D., & Sáiz, A. 2005, Geophys. Res. Lett., 32, L03S02
Brueckner, G. E., et al. 1995, Sol. Phys., 162, 357
Burlaga, L. F. 1988, J. Geophys. Res., 93, 7217
Burlaga, L. F., Sittler, E., Mariani, F., & Schwenn, R. 1981, J. Geophys. Res., 86, 6673
Cargill, P. J., Chen, J., Spicer, D. S., & Zalesak, S. T. 1995, Geophys. Res. Lett., 22, 647
Chen, J. 1996, J. Geophys. Res., 101, 27499
Chen, J., & Garren, D. A. 1993, Geophys. Res. Lett., 20, 2319
Chen, J., & Krall, J. 2003, J. Geophys. Res., 108, 1410
Chen, J., Slinker, S., Fedder, J. A., & Lyon, J. G. 1995, Geophys. Res. Lett., 22, 1749
Chen, J., et al. 1997, ApJ, 490, L191
———. 2000, ApJ, 533, 481
Chen, P. F., & Shibata, K. 2000, ApJ, 545, 524
Cheng, C. Z., Ren, Y., Choe, G. S., & Moon, Y.-J. 2003, ApJ, 596, 1341
Chi, P. J., Russell, C. T., Foster, J. C., Moldwin, M. B., Engebretson, M. J., & Mann, I. R. 2005, Geophys. Res. Lett., 32, L03S07
Degenstein, D. A., Lloyd, N. D., Bourassa, A. E., Gattinger, R. L., & Llewellyn, E. J. 2005, Geophys. Res. Lett., 32, L03S11
Delaboudinière, J.-P., et al. 1995, Sol. Phys., 162, 291
Fedder, J. A., Slinker, S. P., Lyon, J. G., Russell, C. T., Fenrich, F. R., & Luhmann, J. G. 1997, Geophys. Res. Lett., 24, 2491
Garren, D. A., & Chen, J. 1994, Phys. Plasmas, 1, 3425
Goodrich, C. C., Sussman, A. L., Lyon, J. G., Shay, M. A., & Cassak, P. A. 2004, J. Atmos. Sol.-Terr. Phys., 66, 1469
Gopalswamy, N., Barbieri, L., Lu, G., Plunkett, S. P., & Skoug, R. M. 2005, Geophys. Res. Lett., 32, L03S01
Gosling, J. T., & Riley, P. 1996, Geophys. Res. Lett., 23, 2867
Hu, Q., Smith, C. W., Ness, N. F., & Skoug, R. M. 2005, J. Geophys. Res., 110, A09S03
Kivelson, M. G., & Russell, C. T. 1995, Introduction to Space Physics (New York: Cambridge Univ. Press)

Krall, J., & Chen, J. 2005, ApJ, 628, 1046
Krall, J., Chen, J., Duffin, R. T., Howard, R. A., & Thompson, B. J. 2001, ApJ, 562, 1045
Krall, J., Chen, J., & Santoro, R. 2000, ApJ, 539, 964
Landau, L. D., & Lifshitz, E. M. 1960, Electrodynamics of Continuous Media (New York: Pergamon)
Lin, J., Forbes, T. G., Isenberg, P. A., & Démoulin, P. 1998, ApJ, 504, 1006
Lindsay, G. M., Luhmann, J. G., Russell, C. T., & Gosling, J. T. 1999, J. Geophys. Res., 104, 12515
Linker, J. A., Lionello, R., Mikić, Z., & Amari, T. 2001, J. Geophys. Res., 106, 25165
Looper, M. D., Blake, J. B., & Mewaldt, R. A. 2005, Geophys. Res. Lett., 32, L03S06
Lyon, J. G., Fedder, J. A., & Mobarry, C. M. 2004, J. Atmos. Sol.-Terr. Phys., 66, 1333
Manchester, W. B., IV, Gombosi, T. I., Roussev, I., Ridley, A., De Zeeuw, D. L., Sokolov, I. V., & Powell, K. G. 2004, J. Geophys. Res., 109, A02107
McComas, D. J., Bame, S. J., Barker, P., Feldman, W. C., Phillips, J. L., Riley, P., & Griffee, J. W. 1998, Space Sci. Rev., 86, 563
Mikić, Z., & Linker, J. A. 1994, ApJ, 430, 898
Pallamraju, D., & Chakrabarti, S. 2005, Geophys. Res. Lett., 32, L03S10
Riley, P., Linker, J. A., Mikić, Z., Odstrcil, D., Zurbuchen, T. H., Lario, D., & Lepping, R. P. 2003, J. Geophys. Res., 108, 1272
Rust, D. M. 1994, Geophys. Res. Lett., 21, 241
Scherrer, P. H., et al. 1995, Sol. Phys., 162, 129
Seppälä, A., Verronen, P. T., Kyrölä, E., Hassinen, S., & Backman, L. 2004, Geophys. Res. Lett., 31, L19107
Skoug, R. M., Gosling, J. T., Steinberg, J. T., McComas, D. J., Smith, C. W., Ness, N. F., Hu, Q., & Burlaga, L. F. 2004, J. Geophys. Res., 109, A09102
Slinker, S. P., Fedder, J. A., Chen, J., & Lyon, J. G. 1998, J. Geophys. Res., 103, 26243
Slinker, S. P., Fedder, J. A., Emery, B. A., Baker, K. B., Lummerzheim, D., Lyon, J. G., & Rich, F. J. 1999, J. Geophys. Res., 104, 28379
Smith, C. W., L'Heureux, J., Ness, N. F., Acuña, M. H., Burlaga, L. F., & Scheifele, J. 1998, Space Sci. Rev., 86, 613
Sojka, J. J., Schunk, R. W., Bowline, M. D., Chen, J., Slinker, S., & Fedder, J. A. 1997, J. Geophys. Res., 102, 22209
Sojka, J. J., Schunk, R. W., Bowline, M. D., Chen, J., Slinker, S., Fedder, J. A., & Sultan, P. J. 1998, J. Geophys. Res., 103, 20669
Titov, V. S., & Démoulin, P. 1999, A&A, 351, 707
Tsurutani, B. T., et al. 2005, Geophys. Res. Lett., 32, L03S09
Wang, W., Wiltberger, M., Burns, A. G., Solomon, S. C., Killeen, T. L., Maruyama, N., & Lyon, J. G. 2004, J. Atmos. Sol.-Terr. Phys., 66, 1425
Wiltberger, M., Wang, W., Burns, A. G., Solomon, S. C., Lyon, J. G., & Goodrich, C. C. 2004, J. Atmos. Sol.-Terr. Phys., 66, 1411
Wood, B. E., Karovska, M., Chen, J., Bruekner, G. E., Cook, J. W., & Howard, R. A. 1999, ApJ, 512, 484
Woods, T. N., et al. 2004, Geophys. Res. Lett., 31, L10802
Wu, S. T., Guo, W. P., Michels, D. J., & Burlaga, L. F. 1999, J. Geophys. Res., 104, 14789
Yurchyshyn, V., Hu, Q., & Abramenko, V. 2005, Space Weather, 3, S08C02
Yurchyshyn, V. B., Wang, H., Goode, P. R., & Deng, Y. 2001, ApJ, 563, 381
Zurbuchen, T. H., Gloeckler, G., Ipavich, F., Raines, J., Smith, C. W., & Fisk, L. A. 2004, Geophys. Res. Lett., 31, L11805